SET-UP ANALYSIS AND OPTIMIZATION OF CFD SIMULATIONS FOR RADIAL TURBINES

J. Galindo [#], S. Hoyas [#], P. Fajardo *[#] and R. Navarro [#]

* *Bioingeniería e Ingeniería Aeroespacial, Universidad Carlos III de Madrid, 28911 Leganés, Spain.*
E-Mail: pablo.fajardo@uc3m.es (Corresponding Author)
[#] *CMT - Motores Térmicos, Universitat Politècnica de València, Camino de Vera S/N,*
46022 Valencia, Spain

ABSTRACT: This paper proposes a CFD method for simulating radial turbocharger turbine flows. A review is presented of the computational model in terms of meshing, mesh movement strategy, and computational algorithm in turbomachinery CFD simulations. A novel local mesh independence analysis is developed for this purpose. This procedure is aimed at distributing the cells more efficiently by selecting suitable cell sizes for the different regions of the domain to optimize the use of the available computational resources. Pressure- and density-based solvers are compared. The influence of the moving-mesh strategy was analyzed, and small differences were observed in the region near the maximum efficiency point, while these differences increased when off-design conditions were considered. Finally, a comparison of the results with data from an experimental test bench shows that the proposed computational methodology can be used to characterize radial turbomachinery. The objective of the analysis and the optimization of the case configuration was to establish some general guidelines for CFD turbomachinery simulations.

Keywords: CFD simulation, turbocharging, radial turbine, local mesh independence

1. INTRODUCTION

The energy of the exhaust gases from an internal combustion engine (ICE) is approximately 30-40 % of the chemical energy released by the combustion. These gases can be expanded in the turbocharger turbine to drive the compressor. The compressor's task is to increase the density of the air admitted to the cylinder, thereby increasing the engine power output or allowing the engine size to be reduced without decreasing the power output. The latter technique is known as *downsizing*.

There is therefore a strong interest in optimizing the performance of turbomachines. To this end, researchers in the field have focused on understanding the fluid dynamic processes involved in a turbomachine (Japikse and Baines, 1997 and Baines, 2005) using either experimental or computational methods. Experimental research is carried out by testing the turbo in a test rig, as in Galindo et al. (2006), Spence et al. (2007), and Rajoo and Martinez-Botas (2008). Alternatively, researchers such as Hiereth and Prenninger (2007) and Decombes et al. (2010) have used CFD to analyze the internal turbine flow. The use of CFD is becoming more widespread due to advances in the development of numerical methods and an increase in achievable computational power.

Some papers in the literature have reported a good agreement between CFD computations and experimental results, including those of Kreuz-Ihli et al. (2000), Dai et al. (2004), Thakker and Hourigan (2005), and Su et al. (2012). Most of the computational studies on turbomachinery employ steady boundary conditions and assume steady flow, as in Simpson et al. (2009). Blanco-Marigorta et al. (2000) used ANSYS-FLUENT to study the influence of the volute geometry and the relative positions of the impeller and volute casing using unsteady simulations but with constant boundary conditions.

However, when the turbine is working under engine-like conditions, the flow at the turbine inlet is far from constant due to the pulses generated in the cylinders (Baines, 2010). Galindo et al. (2013) analyzed the flow in a radial turbine under sinusoidal pulses and Hellström and Fuchs (2008) studied the effect of inlet flow on turbine performance.

The objective of this paper is to analyze and optimize the set-up of 3D CFD turbocharger turbine simulations to maximize their computational efficiency, i.e., to achieve the highest possible resolution with the computational resources available. The second objective is to present some good working practices or guidelines for CFD simulations in

turbomachinery for the industry. To achieve these objectives, an introduction to turbomachinery modeling is given in this section. In Section 2, the experimental methodology is described and a reference set-up for the simulations is defined. In Section 3, a novel procedure for establishing the mesh independence analysis is proposed, in which mesh independence is analyzed locally instead of considering the whole computational domain. Section 4 provides a comparison of the different set-up options, focusing on the solver type and wheel rotation strategy. The results of these analyses are used in Section 5 to obtain the characteristic curves of the turbine, which are compared to the experimental results. The main conclusions of the paper are presented in Section 6.

2. REVIEW OF COMPUTATIONAL APPROACH AND DEFINITION OF REFERENCE SET-UP

3D CFD simulations were performed for the study using the real geometry of a variable geometry radial turbine (VGT), which provides better performance over a wider flow range (Hiereth and Prenninger, 2007) by changing the stator vanes angle. All the computations were carried out using ANSYS-FLUENT code. The experimental measurements were performed on a turbocharger test rig similar to that used by Luján et al. (2002). The experimental facility is briefly described in Section 2.1. The measurements obtained were used to validate the simulation results.

The existence of turbine vanes influences the operating conditions of the turbine; in particular, the interaction between stator and rotor can affect the simulation set-up. This issue will be dealt with later on. The ability to change vane angles introduces a new uncertainty into the simulation because there is no clear method for determining the actual aperture of the stator nozzles once the turbine is assembled in the test rig at either high or low temperatures. While there is some uncertainty due to *play* in the different elements of the mechanism at low temperatures, the deformation of the elements at high temperatures is unknown.

In the process of setting up the case, many different parameters must be considered. Therefore, it seems reasonable to analyze their effects one at a time. A reference case was therefore chosen and used as a baseline to analyze different configuration parameters. All the

computations were performed using the ideal gas law with variable thermal properties.

2.1 Experimental method

Experimental measurements were obtained on a continuous flow bench to characterize the turbine. This facility is formed by two separate flow lines: one feeds the turbine under controlled pressure and temperature, while the second feeds the compressor. The facility includes distinct instruments to independently measure the mass flow at each line. The flow pressure and temperature of the ducts at the inlet and outlet of both the compressor and turbine were also measured (SAE, 1995). Because the simulations were performed assuming adiabatic walls, the turbocharger had to be insulated to minimize heat loss through the walls during the experiments.

Only overall measurements are generally available for automotive turbines, as their size makes it difficult to measure the flow properties in the flow field of vaned turbines such as the one under study. In practical terms, this means that only the pressure ratio, corrected mass flow rate, rotational speed, and enthalpy drop can be obtained for validation.

2.1.1 Angular position

It is also worth mentioning that there is an additional uncertainty when comparing experimental results with simulations due to the position of the VGT nozzle vanes. The variation in the positioning system of the vanes due to the looseness, or play, of the joint introduces uncertainty in the real position being tested. The bottom of Fig. 1 shows the mechanism used to move the stator vanes. The problem involved here is caused by the impossibility of verifying the vane angle once the turbine has been mounted on the test rig.

To estimate the position of the vanes during the test, a calibrated screw was used to move the stator vane rack mechanism such that the vanes could be moved by rotating the screw and the position was estimated by the screw displacement. Some tests were carried out to calibrate the model by disassembling the turbine and measuring the vane angle in different positions. The top of Fig. 1 shows a photo of the stator vanes in the fully open position. The vane position is measured with reference to the radial coordinate passing through the rotation axis, as indicated in Fig. 1. The relationship between the angular position of the vanes with reference to the rack position is shown in Fig. 2.

Fig. 1   Photo of stator vanes in fully open position. The reference radial direction is indicated for each vane.
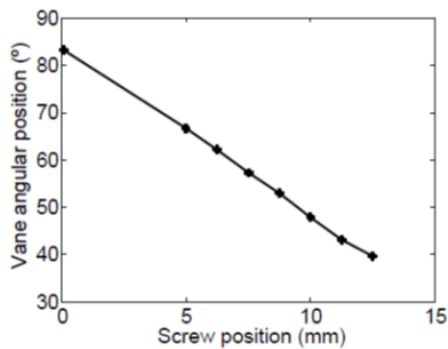

Fig. 2   Evolution of stator vane angular position as function of screw position.

From the results of the angular position, it seems that the behavior of the positioning system is linear. However, some comments need to be made about the positioning system at this point. The first is about the dispersion of the values of the angles of different stator vanes for a given position, which was found to be approximately ± 1°. This effect was not included in the CFD model, in which all the vanes were set at the same angle. The second concerns the previously mentioned play in the positioning mechanism; once the screw position had been set, the vanes could still be manually moved by approximately 5°. Therefore, the angular position of the vanes could change during turbine operation due to the aerodynamic forces on the blades. The play of the
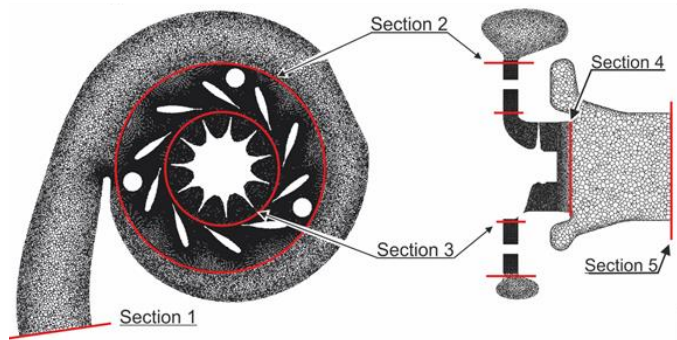

Fig. 3   Schematic representation of turbine geometry and 3D computational mesh for turbine simulations. The different post-processing surfaces are included.

Table 1   Description of post-processing cross-sections considered in the computational domain.

Cross-section number	Description
0	Domain Inlet
1	Volute Inlet
2	Volute Outlet-Nozzle Inlet
3	Nozzle Outlet-Rotor Inlet
4	Rotor Outlet
5	Turbine Outlet
6	Domain Outlet

positioning mechanism may allow thermal expansion of the turbine components at the design operating temperature. There is therefore a degree of uncertainty when comparing the experimental and simulation results, which makes it difficult to validate the computational results. This question will be discussed later on. In the following analysis, the stator position was kept at a constant value of 75 % to reduce the number of parameters involved.

2.2   Computational domain

The computational domain was chosen to represent a turbine mounted on a turbocharger test rig, as in Luján et al. (2002), with straight ducts at the turbine inlet and outlet. Long ducts were therefore used in the computational model, which increases the size of the domain and therefore the computational requirements. To minimize the computational cost, 1D-3D co-simulations are used, as shown in Galindo et al. (2011). The co-simulation limits the use of 3D simulations to the required zones of the domain while computing most of the piping system with a 1D model. Another possible option is to use an anechoic boundary condition that simulates the fluid dynamic behavior of an infinite duct, as in Torregrosa et al. (2012).

In Fig. 3, a sketch of the radial turbine is shown with one of the meshes used in the analysis without the straight inlet and outlet ducts, which are a 100-mm-long, 30-mm-diameter duct upstream of the volute inlet (post-processing cross-section 1) and a 500-mm-long, 40-mm-diameter duct at the turbine outlet (post-processing cross-section 5). To simplify the analysis, the turbine is divided into different regions: volute, nozzles, rotor and outlet. The interfaces between two consecutive regions (see Fig. 3) are used as post-processing surfaces and are numbered correlatively, as shown in Table 1. These numbers were used in the following analyses.

Post-processing cross-sections 0 and 6 are not shown in Fig. 3 because they are located at the farthest ends of the inlet and outlet ducts, respectively. Heat transfer from the turbine was considered negligible due to the insulation of the turbine case and the walls were therefore modeled as adiabatic.

2.3 Boundary conditions

Testing turbochargers under steady-flow conditions, even though it does not faithfully reproduce actual on-engine operating conditions, is the standard procedure followed by manufacturers. All the simulations in the present study were thus performed under steady-inflow conditions using the inlet total pressure and temperature and outlet static pressure as boundary conditions. Another option was to impose the mass flow rate at the inlet instead of the total pressure. However, the combination of total pressure at the inlet and static pressure at the outlet has been found to provide good numerical stability and convergence rates in radial turbine simulations, as shown by Simpson et al. (2009).

2.4 Wheel rotation strategies

One of the most controversial topics in turbomachinery CFD is the strategy for simulating rotor motion. There are basically two different approaches: multiple reference frame (MRF) and sliding mesh model (SMM).

In the former, the mesh does not truly move. Instead, a coordinate system is used that rotates with the rotor, and the flow equations are solved in this rotation reference frame. The Coriolis and centrifugal forces are thus included in the Navier-Stokes equations as source terms. The rest of the turbine, which does not rotate, and the ducts are expressed in a non-rotational (inertial) coordinate system, yielding a steady-state approximation of

the rotor movement. Lam et al. (2002) used this approach to calculate the flow in a turbocharger turbine. The main advantage of using the MRF approach is its relatively low computational cost, as the computation can be performed with a steady solver. However, it cannot take into account typical unsteady flow effects, such as vortex shedding or rotor-stator interactions. In turbomachinery simulations, the multiple reference frame approach may have an impact on the results, as noted by Palfreyman and Martinez-Botas (2005). Liu and Hill (2000) came to a similar conclusion when analyzing different turbocompressors, finding evidence of the importance of the mesh motion model when the stator-rotor interaction needed to be considered. Hillewaert and Van den Braembussche (1999) found that the frozen rotor model was not the most appropriate for radial compressor simulations. In the present work, the MRF simulations were carried out with the *frozen rotor* approach available in ANSYS-FLUENT.

The second approach consists of using the sliding mesh model (SMM), also known as moving mesh, in which one part of the mesh rotates with respect to the stationary part and the two zones are connected by sliding interfaces. Thus, the connectivity for cells on either side of the interface changes at each time step. The SMM is inherently unsteady, which means that the flow variables will continuously oscillate due to blade passing (among other effects). This can be noted in the pressure-wave fluctuations propagated both upstream and downstream of the rotor. The simulation has to be performed until a periodic solution is found. In SMM strategy, the fluctuating pressure waves generated have an effect on the solution due to the non-linearity of the viscous losses, but this is most likely a secondary effect. These waves will also cause spurious reflections when reaching the outlet boundary, which increases the computational time needed to reach a periodic solution. SMM has been proven to give good results (Hellström, 2010).

In the present study, the turbine's rotational speed was kept constant to reduce the number of parameters. The rotational speed selected for the analysis was 18953 rad·s^{-1}.

2.5 Solver type

ANSYS-FLUENT offers two different numerical methods (ANSYS, 2011): pressure-based and density-based solvers. Historically speaking, the density-based approach was developed for high-

speed compressible flows, while the pressure-based approach was used for incompressible and mildly compressible flow. However, both methods have now been extended to solve a wide range of flow conditions beyond their initial intent.

In both methods, momentum equations are used to obtain the velocity field. In the pressure-based approach, a pressure equation is derived by combining the continuity and momentum equations, while the density is calculated using the equation of state. In the density-based solver, the continuity equation is solved to obtain the density field, while the pressure field is determined from the equation of state. The two numerical methods are based on a finite-volume discretization procedure, but the linearization and the approach to solving the discretized equations are different. In general, the density-based method is considered to be more accurate than the pressure-based solver in terms of shock resolution.

2.5.1 Pressure-based solver

As stated above, in the pressure-based solver, a pressure equation is obtained from a combination of the continuity and momentum equations. In this way, the obtained velocity field satisfies the continuity. Due to the nonlinearity and coupled behavior of the flow equations, the solution process involves iterations. Thus, the entire set of governing equations (continuity for the velocity field and pressure equation) is solved repeatedly until the solution converges.

Segregated and coupled pressure-based algorithms are available in ANSYS-FLUENT (ANSYS, 2011). In the segregated algorithm, each of the governing equations is solved independently. In the coupled algorithm, the momentum equations and the pressure-based continuity equation are solved simultaneously. As a general rule, the coupled algorithm has a higher convergence speed than the segregated algorithm. However, the memory requirement for the coupled algorithm is also higher.

2.5.2 Density-based solver

In the same way, two formulations exist under the density-based solver: implicit and explicit methods (ANSYS, 2011). The implicit and explicit density-based formulations differ in the way that they linearize the coupled equations. In the implicit formulation, the unknown value of a given variable in each cell is computed using a relationship that includes both existing and unknown values from neighboring cells. The system of equations for the unknowns is therefore coupled, and these equations must be solved simultaneously. On the other hand, in the explicit formulation, the unknown value for a given variable in each cell is computed using a relationship that includes only the existing values. The equations for the unknown values in each cell can thus be solved one at a time to calculate the unknown quantities.

In summary, the density-based explicit approach solves for all variables cell by cell, while the implicit approach solves for all flow variables in all cells at the same time. Choosing an implicit or explicit solver only applies to the coupled set of flow equations. Transport equations for additional scalars, e.g., turbulence, are solved segregated from the coupled set. The greater stability of the implicit formulation provides a converged steady-state solution much faster than the explicit formulation, although its memory requirements are greater.

When a density-based numerical method is used to obtain steady-state flow solutions, the temporal terms are maintained in the equation. The transient solution is thus computed until a steady-state is reached. This procedure differs from that for pressure-based methods, in which the terms dealing with temporal variation are not included in the discretized equations.

2.5.3 Spatial discretization

A second-order scheme for spatial discretization is adopted for all flow equations. This scheme computes the face values from the discrete values stored in the cell centers for the evaluation of flux terms.

2.6 Turbulence model

With the current computational capacities, a direct numerical simulation in which the whole Navier-Stokes equations are computed is only affordable in simple cases (flat plate, pipes, channels, etc.). In more complex cases, the turbulence needs to be modeled, which constitutes a critical issue in CFD simulations. Different approaches can be followed: Reynolds averaged (RANS) or unsteady Reynolds averaged (URANS) methods in transient simulations or a detached-eddy simulation (DES) (Strelets, 2001) or even a large-eddy simulation (LES) (Smagorinsky, 1963).

Turbomachines are complex fluid dynamic systems in which adverse pressure gradients and flow separation can occur. Many works have been published on the analysis of turbulence models in

turbomachinery simulations. Su et al. (2012) compared RANS and LES for an incompressible case. DES and LES models are considered to be more accurate than RANS because they resolve a part of the turbulence spectrum. However, they have an unaffordable computational cost for the purpose of the current work and other difficulties arise, such as the appropriate definition of the inlet boundary conditions (Tabor and Baba-Ahmadi, 2010). The RANS approach was therefore selected for this work. Aghaei-Tog et al. (2008) analyzed different RANS turbulence models in CFD radial turbomachinery computations. The most commonly used RANS models for internal flow problems are those defined by two equations. Their main advantage is their good trade-off between computational cost and accuracy, such as in Menter's SST turbulence model (Menter, 1994). The SST model blends the robust and accurate formulation of the k-ω model (Wilcox, 1988) in the near-wall region with the free-stream independence of the k-ε model in the far field (Menter, 1992). In the SST turbulence model, the transport of the principal turbulent shear stress is taken into account, which allows the correct response to adverse pressure gradients to be obtained.

The SST model has been used in most of the turbomachinery applications found in the literature. Menter et al. (2004) applied the SST model to turbomachinery simulations and found good agreement between the computations and the experimental data for all cases considered. Another of its applications in turbomachinery simulations can be found in the work by Pecnik et al. (2001), in which the uncertainty of transition prediction is analyzed. Simpson et al. (2009) used the SST in CFD simulations of vaned and vaneless radial turbines, obtaining good results. These examples testify to the model's ability to capture the effects of Reynolds number variations and flow separation over a wide range of conditions. Based on the number of cases in the literature in which the k-ω SST model has provided good results, this model was adopted for the computations in the present study.

2.7 Reference set-up

In the following section, the effect of the mesh size on the results is evaluated to identify the most suitable mesh for the computations. To perform this mesh independence analysis, a reference case must be defined. Apart from the configuration decisions already mentioned in this section, such as the domain geometry and

turbulence model, there are other model set-up choices that have to be made. For computational reasons, the analysis is performed using a pressure-based solver and an MRF strategy for rotor motion. In Section 4, the effect of the case configuration will also be evaluated.

3. LOCAL MESH INDEPENDENCE ANALYSIS

The first thing that must be analyzed when dealing with 3D simulations is the geometry considered, especially the mesh. The mesh should be fine enough to faithfully reproduce the geometry, which is usually achieved by searching for the independence of the solution in terms of the number of cells. The meshes used for the computations in this work are similar to that shown in Fig. 3.

The main difficulty in dealing with real geometries is achieving the appropriate mesh. In this work, a mixed polyhedral and extruded-polygonal non-conformal mesh was used. ANSYS-FLUENT makes it possible to generate a polyhedral mesh from a tetrahedral mesh using the algorithm described in the ANSYS (2009). The greatest advantage of polyhedral meshes is that they are more accurate than the equivalent tetrahedral mesh. In other words, it is possible to achieve the same resolution with fewer cells (FLUENT, 2006). Polyhedral meshes have been used to solve computational problems in engineering, as in Tritthart and Gutknecht (2007), who developed a method for solving Reynolds equations with polyhedral cells, which showed better behavior than quadrilateral cells in certain problems. Baris and Mendonça (2011) used a polyhedral mesh for turbocharger computations and cited less numerical diffusion and a more accurate gradient calculation as the benefits of this type of mesh.

Once the mesh type is chosen, mesh independence analysis should be performed. Mesh independence analysis is usually conducted by considering that finer meshes produce better results due to the discretization error, which decreases with cell size. The usual procedure when dealing with turbomachinery simulations consists of using different meshes with increasingly small cell sizes, as used by Li (2009). This procedure may seem straightforward in the case of a simple system, particularly if the cells are more or less uniformly distributed. However, for a more complex system and if the real geometry is considered, it may not be the most appropriate because not all the subdomains of the

system require the same number of cells. This is the case for the turbine, in which a smaller cell size is preferable in the rotor region, where the momentum interchange occurs, relative to that in the ducts, which can be computed with a one-dimensional approach. The procedure shown here aims to optimize the resources in terms of cell distribution.

It is worth mentioning at this point that even though smaller cells theoretically produce better results, there are other issues that have not been taken into account. One is that if cell refinement has not been properly carried out, it may increase the cell aspect ratio, and the use of distorted cells can introduce convergence errors and even spurious solutions. The other issue is that RANS turbulence models are usually applied in combination with wall functions, which model flow behavior near the wall. Although the k-ω turbulence model was chosen and its *automatic wall treatment* (Esch and Menter, 2003) has the advantage of ensuring a high degree of grid independence, the y^+ values of the cells at the walls must be within the range of application of the wall function, as explained in the ANSYS (2009). A thorough mesh refinement should therefore be performed to prevent cells next to the walls from having y^+ values too low to accurately use the wall functions or too high to resolve the viscous sublayer.

As previously stated, the turbine was divided into four different regions: the volute, stator, rotor, and outlet regions. The local mesh independence analysis proceeds as follows. First, a reference case was defined in terms of the mesh. Each turbine zone was analyzed independently. The influence of mesh size on each region was investigated by changing the grid in this zone only, using the rest of the mesh from the reference case. Simulations were performed with a progressively finer mesh until the variation of the solution of two consecutive cases was sufficiently small, as is the usual procedure in standard mesh independence analysis. At this point, the increase in the computational cost of additional refinements is not justified by the increase in resolution. The process continues with the analysis of the following turbine zone. When all the subdomains have been evaluated, the information obtained can be used to determine the regions most worth refining to obtain a better cell distribution. The numerical set-up described in the previous section is used throughout the mesh independence analysis.

To study the mesh refinement effect, two parameters are analyzed at every refinement level:

mass flow through the current element and total turbine torque. In the following subsections, the meshing procedure and the local mesh independence analysis of each turbine region are described.

3.1 Volute

The volute is designed to feed the stator as uniformly as possible. The volute should therefore be a convergent duct to compensate for the mass flow delivered to the stator and to keep the pressure at the volute-stator interface as constant as possible. As previously mentioned, a polyhedric mesh is used in the volute. Due to the importance of the volute tongue, a smaller cell size in this region might be useful. An ANSYS-FLUENT size function was used centered on the tongue edge, as depicted in Fig. 4. The size function was configured with a minimum dimension of half the default meshing size used for the original tetrahedral grid and a growth rate of 1.1. All the meshes were therefore defined by only one parameter, i.e., the default meshing size. Different volute grid sizes were analyzed, each having approximately twice the number of cells as the preceding one. Information on the size of the volute meshes used is given in Table 2, as is the reference case.
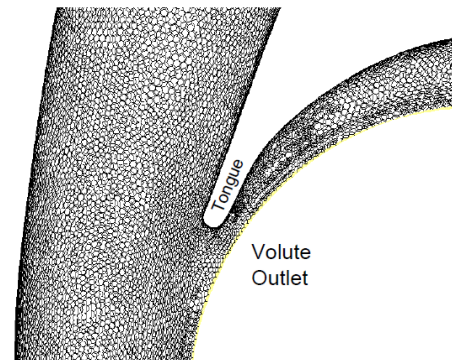

Fig. 4   Close-up of mesh in volute tongue.

Table 2 Size of volute meshes used in mesh independence analysis.

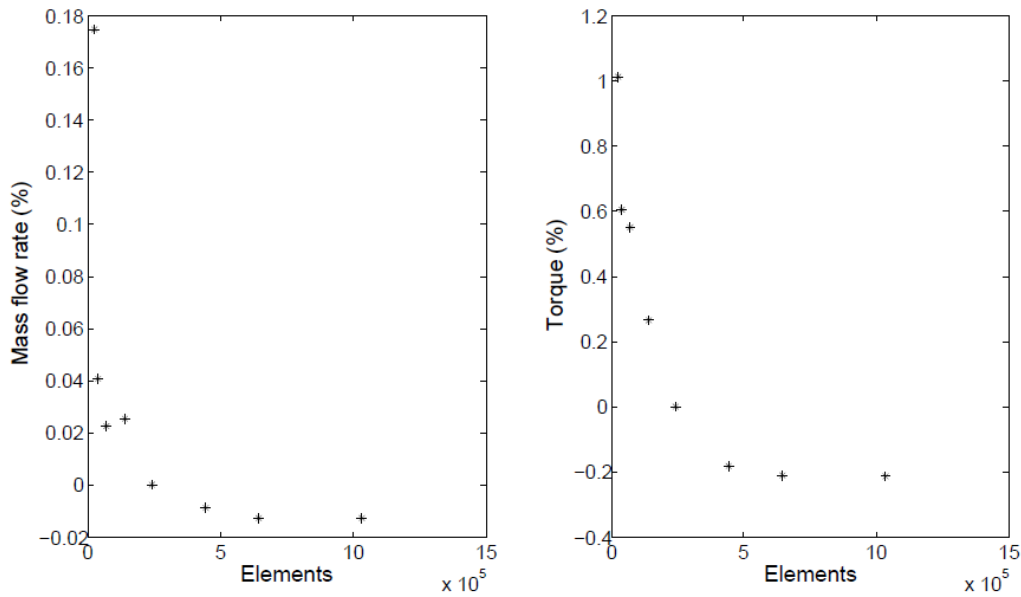| Volute number	Number of polyhedric cells
V0	26491
V1	40267
V2	71613
V3	141022
V4	242443 (reference case)
V5	444760
V6	646077
V7	1034209

Fig. 5   Mesh independence analysis for volute region cells in terms of mass flow rate (left panel) and generated torque (right panel).

Simulations were performed using each of the different volute grids while keeping the rest of the domain meshes as in the baseline case. The results obtained for the different cases are plotted in Fig. 5. The figure shows the variation of mass flow and torque as a percentage of the corresponding parameter of the reference case with the number of elements in the volute. Based on these results, the resolution of the volute region seems to behave as an exponential function. The gain in the last three meshes is less than 0.01 %; however, the difference increases rapidly for the coarser meshes.

3.2   Stator

For the mesh independence analysis and set-up optimization performed in this paper, the stator vanes were set at a constant position. Due to the particular shape of the nozzle region, the stator mesh was defined by two parameters: the cell size used in the stator walls (both upper and lower faces were meshed in the same way), which defines the resolution obtained in the stator vanes; and the number of rows in the transversal direction, which is important for describing the flow profiles in the stator.

The topology chosen for the stator mesh consisted of extruded polygons. This meant that the faces forming the surface mesh on the stator wall were meshed using triangular cells, which were extruded in the transversal direction. ANSYS-FLUENT was then used to convert these triangles into polygons. It seemed to be of interest to have a higher resolution, or finer mesh, in the regions close to the stator vanes and screws; thus, a size function with the same configuration as in the volute was applied to the stator.

The parameters that define the stator meshes used in this analysis in terms of the number of cells in the stator wall and the number of rows in the transversal direction are shown in Table 3.

First, the mesh independence analysis was performed directly using the total number of cells. Some trends can be seen in Fig. 6, showing that if the number of cells is increased, the dispersion of the values decreases. However, it is not clear whether it is better to increase the number of cells in the face or the number of rows.

Table 3   Size of stator meshes used in mesh independence analysis.

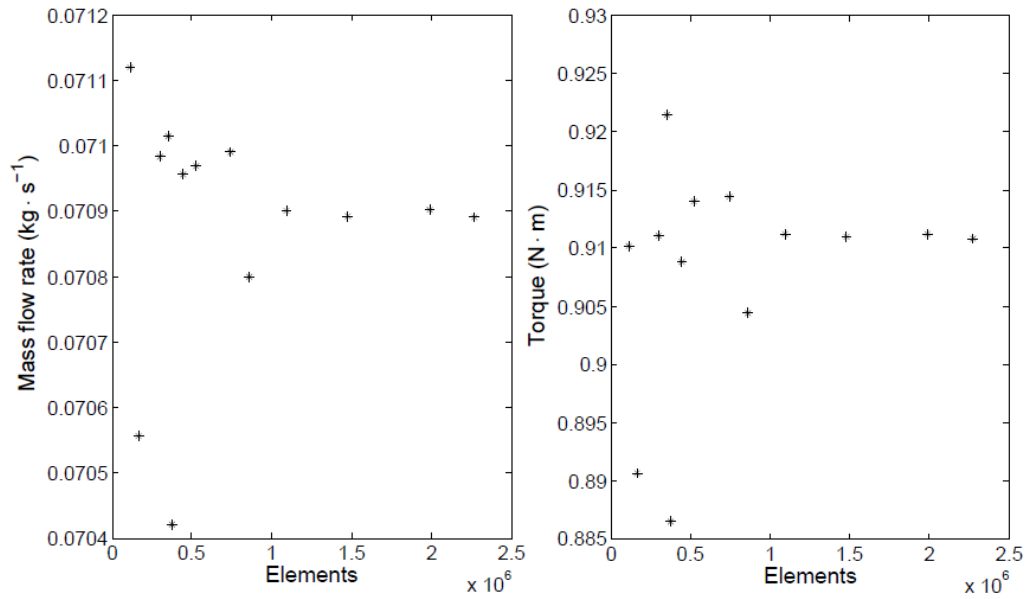| Number of cells in wall	Number of rows	Case number
8743	11	S0
14159	11	S1
	15	S2
	22	S3
24490	10	S4
	15	S5
	22	S6
	30	S7
43396	6	S8
	10	S9
	15	S10
	22	S11
	30	S12
79302	15	S13
	22	S14
	30	S15

Fig. 6   Mesh independence analysis for stator region using total number of cells in terms of mass flow rate (left panel) and generated torque (right panel).
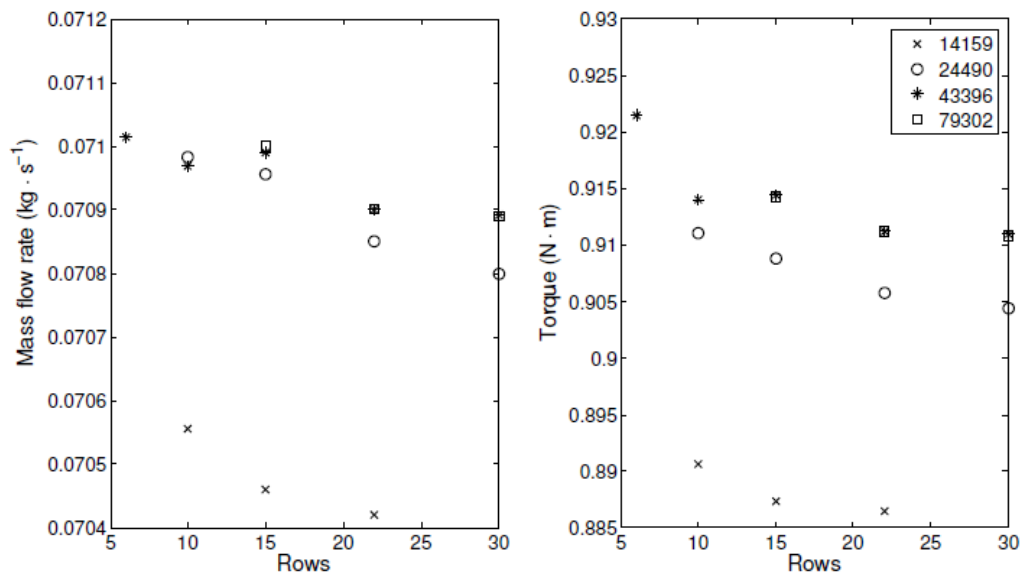

Fig. 7   Mesh independence analysis for stator region using total number of cell rows in terms of mass flow rate (left panel) and generated torque (right panel).

The evolution of the parameters analyzed with the number of rows is shown in Fig. 7. The curves are grouped together according to the number of elements in the stator wall.

From the results, it is clear that for the face meshes with 43396 and 79302 elements, the variation of the mass flow rate and torque with the number of rows is negligible. Additionally, the increase in computational cost from 15 to 30 transversal rows does not justify the approximately 0.4 % change in the solution for the torque developed by the turbine. The intermediate value of 22 rows may be a good trade-off solution.
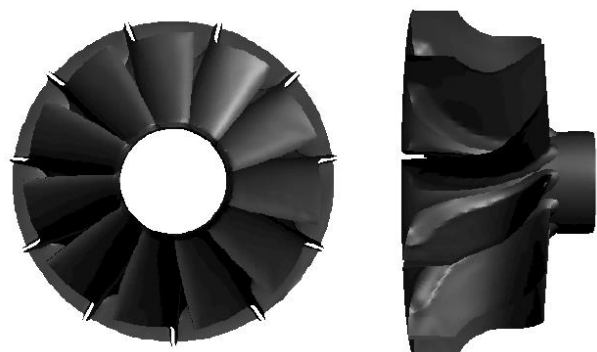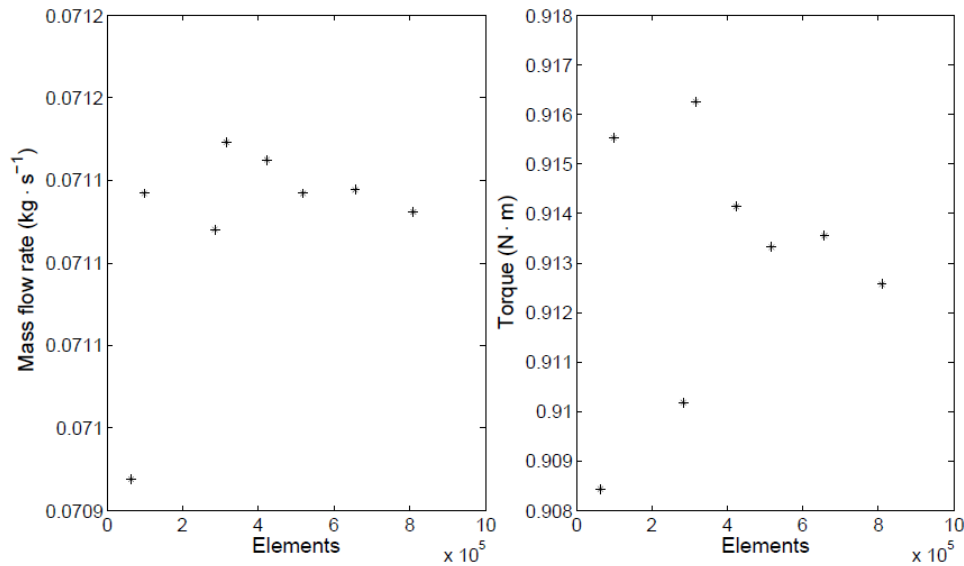

Fig. 8   Close-up of rotor zone geometry.

Fig. 9   Mesh independence analysis for rotor region using number of cells in terms of mass flow rate (left panel) and generated torque (right panel).

A small volume is used between the stator and rotor regions. This volume goes from the end of the stator vanes to the rotor inlet cross-section, as seen in Fig. 3. This volume was meshed using hexahedral cells with the same face size as in the stator. In the final mesh, the number of elements in this transition stator rotor region is included as part of the stator.

3.3   Rotor

The rotor region, due to its shape, is the part of the original geometry where the effects of working with real digitalized geometries are most noticeable, as seen in Fig. 8 in the different fillet radii in the rotor blades, which makes a polyhedric mesh more appropriate for the rotor region. Following the same criteria as in the previous turbine regions, a size function was used to increase the resolution close to the walls. The configuration was similar to that used for the volute and stator. The total number of elements was thus defined with the default meshing size, as in the volute. The different rotor meshes used in the analysis are given in Table 4.

The results obtained for rotor mesh independence in terms of mass flow rate through the rotor and generated torque are shown in Fig. 9. In this case, the independence curve has a different shape than in the previous analyses. The curve obtained for the volute had a typical *overdamped* shape. However, the rotor presents stronger oscillating behavior and the curve *overshoots*, i.e., exceeds the equilibrium level at each oscillation, while also decreasing in total amplitude.

This oscillating behavior made it necessary to increase the number of points in this analysis to

Table 4   Size of rotor meshes used in mesh independence analysis.

Rotor number	Number of polyhedric cells
R0	64655
R1	99662
R2	285001 (reference case)
R3	315943
R4	423821
R5	518067
R6	657259
R7	810716

ensure that no spurious aliasing effect would be obtained. If only four points had been acquired, the behavior obtained may have been completely different, leading to an erroneous result. The difference between the last points of the analysis was approximately 0.2 %. It is worth noting that for the rest of the local mesh independence analyses, the torque prediction depends on the refinement level due to variations in the flow conditions at the rotor inlet. However, in the case of the rotor, this effect is combined with the variation in the torque computation due to the refinement of the impeller. In fact, if a torque parameter is defined relating the torque developed by the turbine (T_T) to the flow variables at the rotor inlet,

$$C_m = \frac{T_T}{1/2\rho U_{rotor}^2} \tag{1}$$

and is used as a parameter for the mesh independence analysis, the oscillating behavior does not appear, as seen in Fig. 10. Using the torque parameter, the influence of the inlet
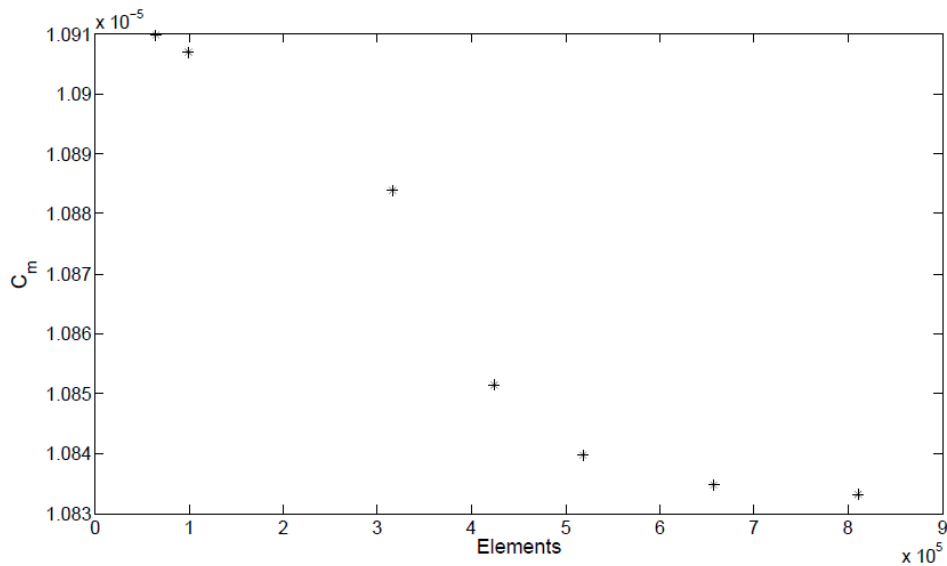
Fig. 10   Evolution of torque coefficient with number of cells in turbine rotor region.
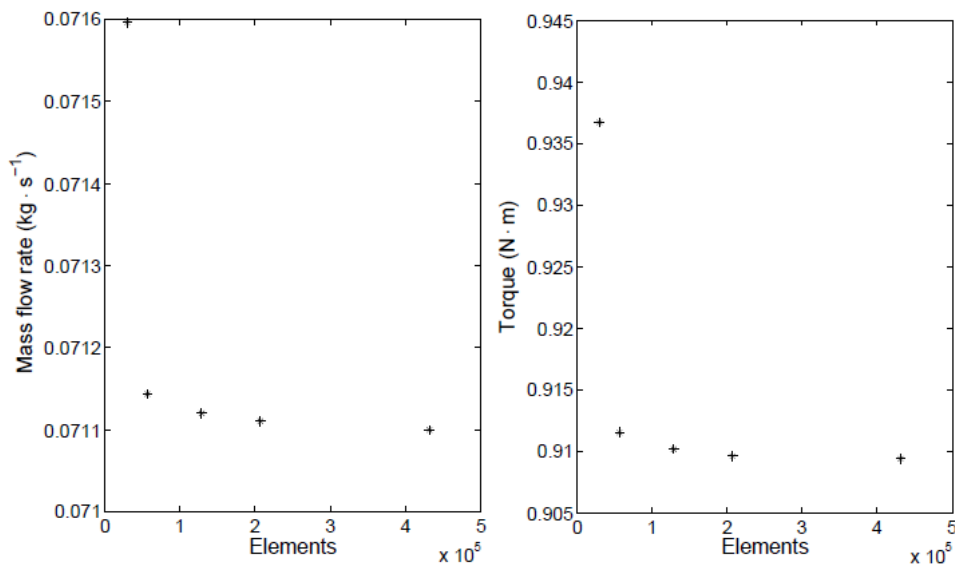

Fig. 11   Mesh independence analysis for outlet region using total number of cells in terms of mass flow rate (left panel) and generated torque (right panel).

conditions on the calculated torque is reduced; thus, the torque accuracy is only determined by the accuracy of predicting the exchange of momentum with the rotor walls.

3.4   Outlet region

The turbine outlet region lies between the rotor outlet and the turbine outlet (Sections 4 and 5 in Fig. 3). As in previous cases, different mesh sizes were used in the outlet region, and a uniform tetrahedral mesh was used for the subsequent conversion to polyhedra. The various meshes are described in Table 5.

The results obtained for the outlet region mesh independence in terms of the mass flow rate through the cross-section and the torque generated by the turbine are shown in Fig. 11, which shows

Table 5   Size of outlet region meshes used in mesh independence analysis.

Outlet region number	Number of polyhedric cells
O0	29281
O1	56392
O2	128671 (reference case)
O3	207451
O4	432179

a very pronounced trend. In the meshes with more than 10^5 elements, the parameters change little. However, the meshes with fewer elements do show large variations.

3.5   Final considerations and selected mesh

The local mesh independence of the different turbine components was analyzed in the previous

subsections. From these results, it is possible to establish the best cell distribution between the different turbine zones according to the computational resources available. However, a number of points should be made before proceeding.

First, the current analysis was performed by separating the influence of the different components. If a final mesh resolution of approximately 1 % accuracy is sought, the relative error in each of the components should be lower (a limit of approximately 0.2 % was considered in this work) to remain on the conservative side.

The analysis was performed by assuming that the behavior of the different components was independent to justify the procedure used, in which the local mesh independence of each component was studied by replacing only that region of the mesh in a reference case and thus all the variations between the different simulations were attributed to the replaced zone. However, it is not clear that if mesh independence has been achieved using the rest of the regions in the reference case, it will also be independent once all the regions have been changed to the refined mesh. To ensure the independence of the final mesh, some additional simulations were performed, substituting each of the mesh components for the finest one used in the previous analysis. The effect of the reference case was assessed in this way. In the simulations performed after refining the different zones in the selected mesh, the solution varied by less than 0.2 % in terms of mass flow and torque, thus ensuring mesh independence.

Finally, the inlet and outlet ducts were not included in the mesh independence analysis. The inlet and outlet were meshed using a cell size similar to that used in the volute, and an extruded scheme was used to mesh the volume.

3.5.1 Final mesh

From the results of the mesh independence analysis, the following meshes were chosen for each of the components:

It is important to emphasize here that the mesh selected for the stator was the one with 43396 cells in the stator wall and 22 rows in the transversal direction. The number of elements in the ducts is not included in Table 6, but the cells are counted in the total number of elements. The inlet duct contains approximately 1.2 % of the total cells, while the outlet duct contains approximately 4.9 %. The total number of cells

Table 6 Number of elements in mesh of different turbine components for mesh selected using mesh independence analysis.

Zone	Number of polyhedric cells (%)	Average cell volume (mm^3/cell)
Volute	646077 (23.3 %)	0.21
Stator	1094812 (39.5 %)	0.017
Rotor	657259 (23.6 %)	0.017
Outlet region	207451 (7.5 %)	0.40
Total number of elements	2777122	0.090

for the turbine alone is 2605599. The last column in Table 6 provides the average cell volume (mm^3/cell) in each turbine zone. As expected, the cell size required in the volute is larger than that obtained for the stator and rotor.

4. SET-UP COMPARISON

After selecting the appropriate mesh, the computational cases must be configured. Different parameters must be considered in this procedure. The most important of these parameters for the case of turbomachinery simulations are the moving mesh strategy, the solver used in the simulations, and the temporal discretization. This section compares the effect of the different configurations.

4.1 Type of solver

Simulations were carried out with different mesh sizes to compare the behavior of pressure- and density-based numerical methods. These calculations were performed using the multiple reference frame approach to simulate rotor motion. The results were compared in terms of the corrected mass flow and the power developed by the turbine. The turbine corrected mass flow is defined as

$$\dot{m}^* = \frac{\dot{m}\sqrt{\dfrac{T_t}{T_0}}}{\dfrac{p_t}{p_0}} \qquad (2)$$

Hereinafter, the corrected mass flow is based on a pressure (p_0) of 101325 Pa and a temperature (T_0) of 288.15 K. The results of the different simulations are shown in Fig. 12.

Certain conclusions can be drawn from the results. First, although the ANSYS-FLUENT user's manual maintains that both solvers are
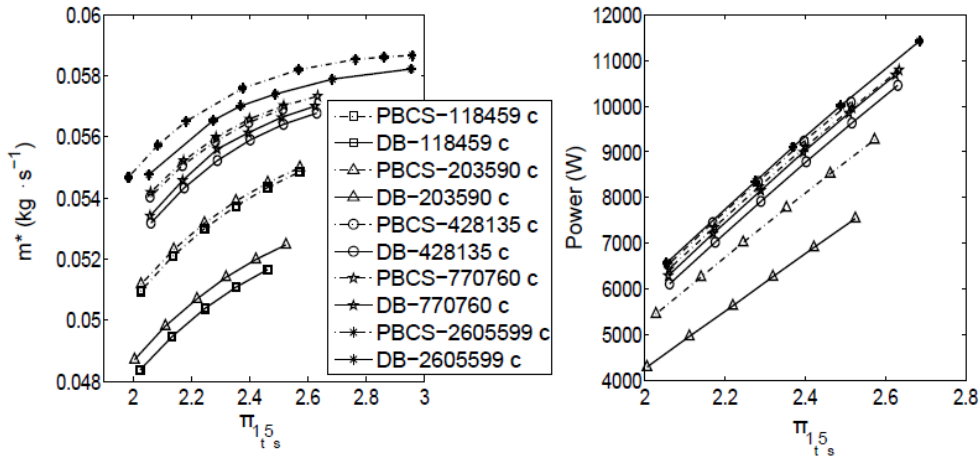
Fig. 12 Comparison between pressure-based coupled (PBCS) and DB solvers in terms of flow capacity (left panel) and turbine power (right panel) vs pressure ratio for different meshes.

valid for all flow regimes, the results obtained are quite different. It is interesting to observe that for different mesh sizes, the pressure-based coupled solver gives a higher flow capacity than the density-based solver. Second, it seems that the relative error between both solvers decreases as the number of cells increases. In the same way, the relative difference between two consecutive mesh sizes also decreases. The 2605599-cell mesh obtained from the mesh independence analysis described in the previous section had a relative error between the PBCS and DB results of less than 1 %. Finally, it is interesting to note that a single steady (MRF) point with the DB solver for the finest mesh required approximately 1 month of computation using the computational resources at our disposal, while the PBCS solver needed only approximately 1/10 of that time. This finding alone justifies using the PBCS in the simulations.

4.2 Mesh motion strategy

A description of the different moving mesh strategies was given in Section 2.4. This section compares the computational results obtained from both rotor motion approaches.

Some of the studies on turbomachinery simulations in the literature used the MRF approach, e.g., Lam et al. (2002). The movement of the mesh adds a high computational cost but may be necessary if the rotor-stator interaction is strong. This effect was analyzed by Liu and Hill (2000) for the case of a turbocompressor. Simpson et al. (2009) showed that the SMM solutions gave better results than the MRF for radial turbines. Other authors, such as Hellström and Fuchs (2009), Palfreyman and Martinez-Botas (2005), and Kawakubo (2010), reached the
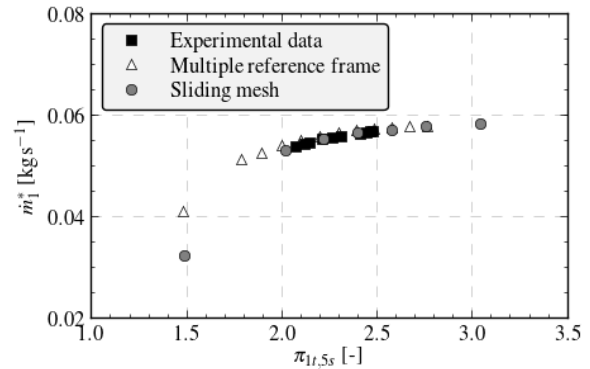

Fig. 13 Flow capacity curves of radial turbine. Corrected mass flow vs overall pressure ratio.

same conclusion. However, it is still one of the most controversial points in turbomachinery simulations, as seen in the work by Aymanns et al. (2011), in which the MRF approach is used, even for pulsating flow.

Fig. 13 shows the results obtained from the MRF and SMM moving mesh approaches. In this case, both computations were performed using the same mesh and the same solver (PBCS) to isolate this effect. The results were compared with the experimental measurements from the testing facility. In the figure, π_{1t5s} represents the ratio between the total pressure on post-processing cross-section 1 (see Fig. 3) and the static pressure in Section 5. $\dot{m}_1^*$ is the corrected computed mass flow, computed using Eq. (2), in post-processing cross-section 1.

Based on the results given in Fig. 13, both methods give similar flow capacity results, with a difference of approximately 5 %, for the higher-pressure-ratio points (design points). However, the curves differ by up to 25 % for the points from the off-design condition, which could be due to a stronger stator-rotor interaction.

As previously stated, there is an uncertainty in positioning the stator at the desired aperture, which made it difficult to acquire experimental data to validate the computations. The procedure applied to compare the experimental points was as follows: the turbine installed in the test rig was set at a given pressure ratio, and the stator aperture was changed by adjusting the rack of the positioning system until the corrected mass flow matched the previously computed value. Once the stator position had been set, a complete curve was obtained for the rotational speed considered. The most common presentation of the turbine performance is in terms of an efficiency defined as

$$\eta = \frac{P}{P_{is}}, \tag{3}$$

where P is the actual power developed by the turbine and P_{is} is the isentropic power, i.e., the maximum power that could be developed by the turbine under ideal conditions at the same operational point. The results obtained in MRF and SMM for turbine efficiency are shown in Fig. 14. The definition of efficiency is clear for the steady cases performed in the current work, but this is not the case for pulsating flows as in Galindo et al. (2013). In that work, the power developed by the turbine is therefore used instead. Fig. 15 shows the turbine torque evolution as a function of pressure ratio. It is worth mentioning that in this analysis, the power generated in the turbine is equivalent to the torque because the rotational speed was kept constant. Once again, there is a difference between the results in Figs. 14 and 15 computed using both techniques, e.g., the turbine efficiency varies by up to 11 %. There is an additional difficulty when trying to validate the computational results because only a narrow range of experimental data might be obtained, and the off-design points, where the differences are greater, may not be evaluated. It seems that there is a better correlation between the experiments and the computations obtained from the SMM than the MRF. The effect of the moving mesh strategy under different operating conditions is shown in the rotor flow fields plotted in Fig. 16. The figure shows the velocity contours and vectors at the mid-span surface of the rotor. It is clear that for the cases modeling a pressure ratio of 2.8 (180 kPa relative total pressure at the inlet), the solution obtained with both strategies is quite similar. Conversely, in the off-design condition, e.g., a pressure ratio of 1.5 (40 kPa relative inlet total pressure), the flow behavior is quite
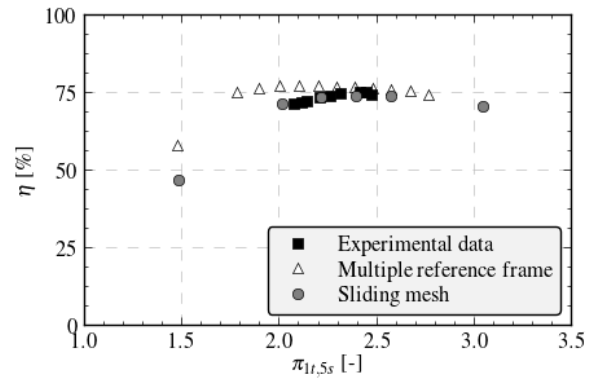

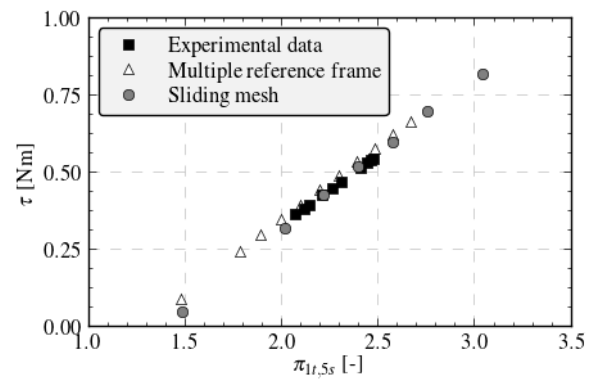Fig. 14 Performance curves of radial turbine in terms of turbine efficiency.

Fig. 15 Performance curves of radial turbine in terms of torque developed.

different. Finally, it is worth mentioning that approximately 50 rotor revolutions were required (over two months of computational time) for a single SSM computation to reach a periodic regime. Hence, the MRF approach could be used if the design operating conditions are modeled, but SMM is necessary when simulating off-design conditions, in which the stator-rotor interaction is stronger.

4.3 Temporal discretization

The last topic to be covered in this section is the temporal discretization of the equations. SMM needs the simulation to be under transient conditions because the mesh is actually moved, therefore requiring a transient discretization of the equations. Temporal discretization involves integrating the terms of the differential equations over a time step, Δt, which needs to be defined. Among the time-discretization options available in ANSYS-FLUENT, the first step is to decide whether to use an implicit or explicit approach. In explicit time discretization, the time step is restricted to the stability limit of the underlying solver (i.e., CFL condition). This criterion would give a different time step in each cell of the domain. However, because all the cells in the
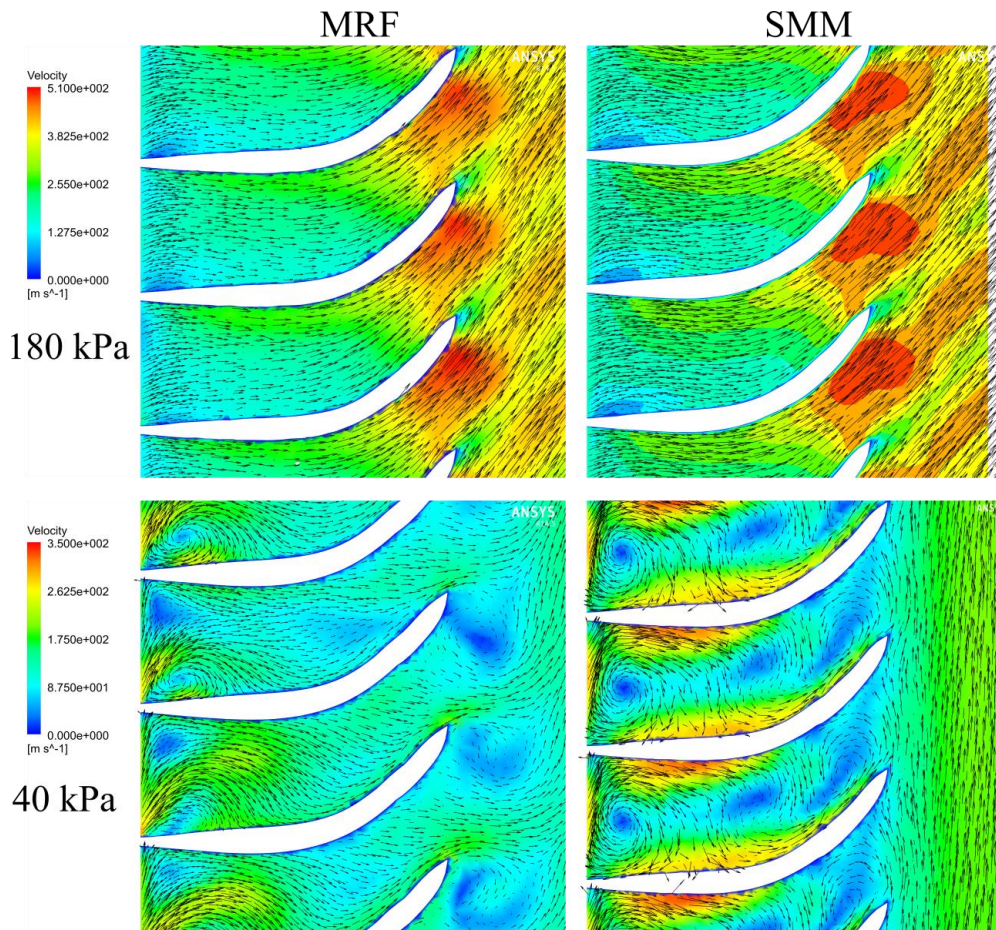
Fig. 16   Comparison of flow field in turbine rotor for two operating conditions (180 kPa and 40 kPa) and two moving mesh strategies studied.

domain should use the same time step, the selected time step must be the minimum of all the local time steps in the domain. The use of explicit time stepping is quite restrictive and leads to time steps on the order of 10^{-9} for the case of the turbine, which is unaffordable using the available computer resources. Moreover, explicit time discretization is only available for the density-based solver, which represents a further increase in computational time. Implicit time discretization was therefore selected for the current work.

The advantage of the fully implicit scheme is that it is unconditionally stable with respect to time-step size, as described in the FLUENT Theory Guide (2011). In this case, the time step is not obtained from the application of a stability criterion and needs to be selected. The influence of time-step size is analyzed in the following sub-section.

4.3.1   Time-step size

According to the ANSYS-FLUENT user's guide (2009), as a general criterion in resolving the transient behavior of blade passing, approximately 10-20 time steps per blade passing

should be allowed. This time-step size is of the same order as other time steps adopted in the literature, as in Simpson et al. (2009), in which the impeller mesh turns 1° per time step. In the current simulations, a size of 200 time steps per rotor revolution was considered as the first approach. Therefore, given the rotational speed of the impeller of 18953 rad·s^{-1}, a time-step size of $1.6576 \cdot 10^{-6}$ s was chosen. In this subsection, a sensitivity analysis of the effect of the time-step size is performed.

The unsteadiness of the SMM simulation can be seen by plotting the turbine torque history, as shown on the left panel of Fig. 17. The oscillations correspond to the unsteady behavior of the internal flow in the turbine. The oscillations due to impeller rotation and blade passing can be identified in the frequency spectrum. The main frequency of the impeller rotation can be computed as

$$f_{Rotor} = \frac{\omega}{2\pi} = 3016.46 \, \text{Hz}. \qquad (4)$$

This line is marked in the frequency spectrum plotted on the right panel of Fig. 17. The first
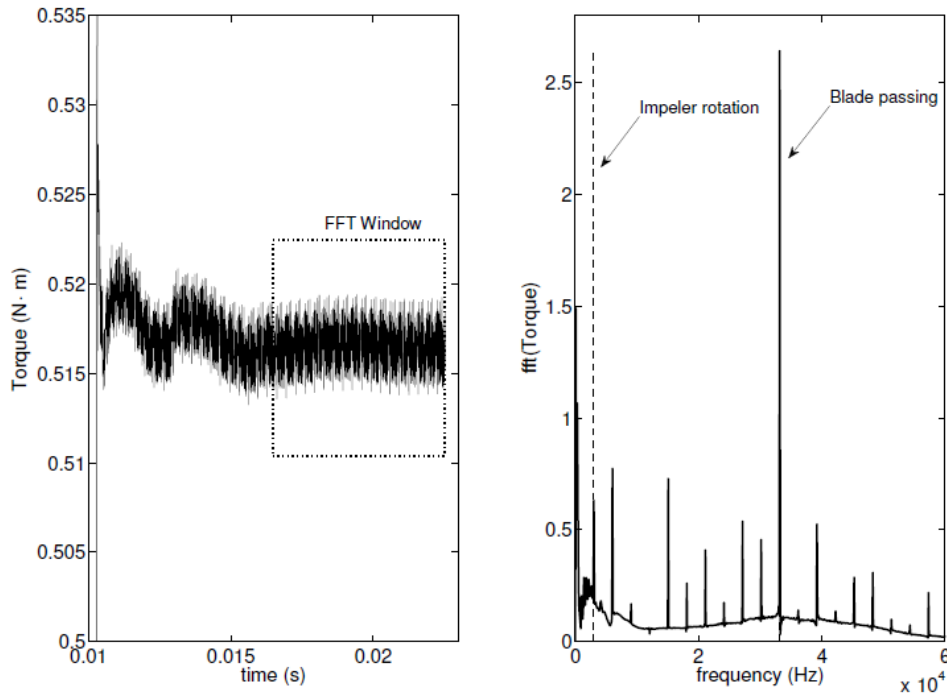
Fig. 17   Temporal evolution of torque developed by turbine (left panel) and the corresponding FFT (right panel).

Table 7   Analysis of influence of time-step size.

Time step (s)	Mean value variation (%)	Amplitude of oscillations (%)
$1.6576 \cdot 10^{-6}$	-	1.05 %
$3.3152 \cdot 10^{-6}$	1.45 %	0.77 %
$8.288 \cdot 10^{-7}$	1.24 %	1.42 %

cycles of the signal are discarded to include only the periodic part of the signal, as indicated on the right panel of Fig. 17. The FFT was then computed by applying a Hamming window to the signal. The other characteristic frequency, which is in fact the one with the highest amplitude, depends on the rotor blade passing. Because there are 11 blades, the frequency is 33181.1 Hz. An analysis of the variation of the mean value of the torque and the amplitude of the oscillations with respect to time-step size is given in Table 7.

The results are shown in terms of the percentage variation of the mean value of the torque developed by the turbine with respect to the torque obtained with the initial time-step size. The oscillations are also given as a percentage of the respective mean value. The mean value error tends to decrease with time-step size. However, dividing the time-step size by two doubles the computational requirements, and a single SMM computation took over two months. A time-step size of $1.6576 \cdot 10^{-6}$ s was therefore selected for the rest of the transient computations because doubling the computational time was clearly unaffordable.

5.   SUMMARY OF THE RESULTS: TURBINE MAP

In the previous sections, a mesh independence analysis was described in Section 3, and the optimization of the case configuration was given in Section 4. The analysis of the set-up showed that pressure- and density-based solvers give different results but tend to converge as the mesh is refined. When dealing with the mesh motion strategy, two different approaches were analyzed, revealing that the results are similar in the design range. However, the differences increase as the flow condition moves away from the design region, as shown in Fig. 13. It can be concluded that the MRF, due to its low computational cost, is a good choice for obtaining the first approach of the solution if the points considered are close to the design conditions. On the other hand, if off-design points are evaluated, the rotor-stator interactions effects are higher; thus, a fully unsteady SMM simulation is required.

The turbine analyzed was a VGT, which means that the angle of the stator vanes could be varied to change its effective area to increase the turbocharger transient performance. The analysis was conducted using a constant aperture angle in the stator. In this section, the turbine maps are obtained for different apertures to analyze their effect on turbine behavior. The numerical results were compared to those acquired from the test bench. The experimental measurements could only be performed in a narrow range close to the
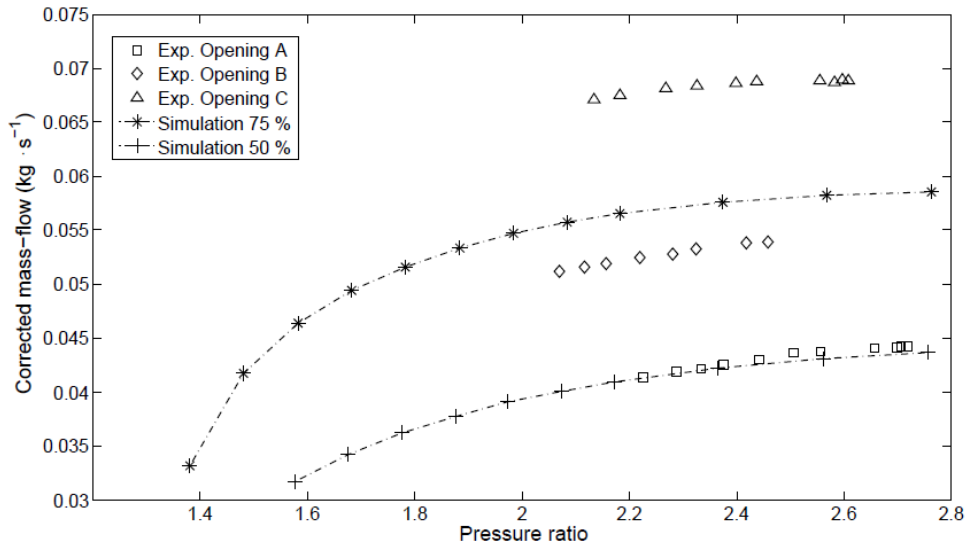
Fig. 18 Turbine flow capacity for different nozzle apertures, showing three experimental and two simulated apertures.
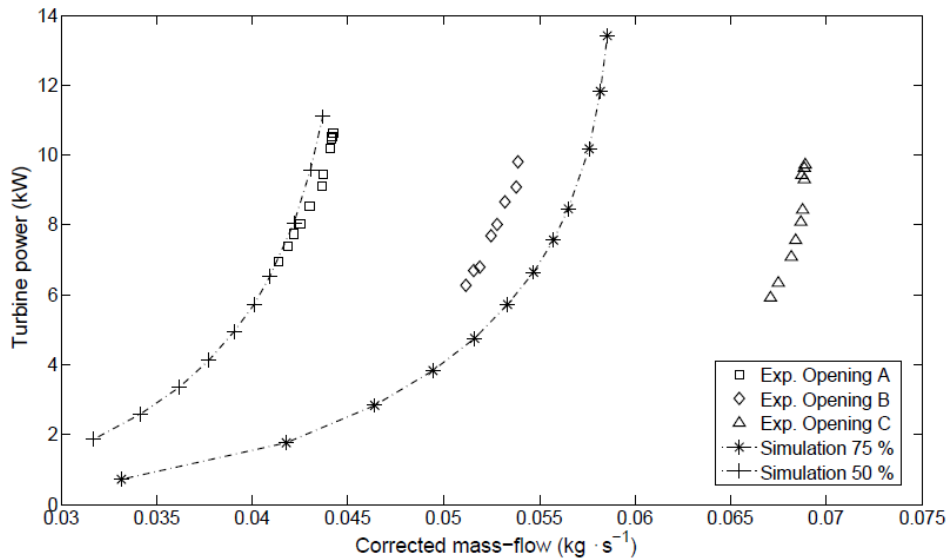

Fig. 19 Turbine performance in terms of power versus mass flow parameter, showing three experimental and two simulated apertures.

design conditions; therefore, the simulations used the MRF strategy to reduce the computing time. The results obtained in terms of flow capacity are given in Fig. 18.

The nozzle aperture increases the flow capacity for the same pressure ratio. As stated above, there is an additional uncertainty in the actual value of the angle of the stator vanes, which makes it difficult to compare the experimental and numerical results. However, all the curves obtained follow the same trend. The results from experimental opening **A** and the 50 % opening simulations are in good agreement.

To describe the turbine behavior, two different curves should normally be provided: one representing turbine flow capacity, as shown in Fig. 18, and another dealing with the torque or power generated by the turbine.

Fig. 19 shows the power developed by the turbine versus the mass flow parameter. The use of this parameter is equivalent to the corrected mass flow because the only differences are the reference pressure (101325 Pa) and temperature (288.15 K). Because the curves are normally acquired at constant speed, torque and power are equivalent quantities. The results show that all the curves have a similar trend, with the only variation being in the effective area. Additionally, the curves obtained for experimental opening **A** and the 50 % aperture simulation show good agreement. It should be remembered that the corrected mass flow and power obtained with the MRF approach were slightly overestimated (approximately 7 % for power), as shown in Figs. 13, 14, and 15. If this overestimation is taken into account, the agreement would be even better if SMM were

used. Due to the similarity between the experimental and numerical results, the method developed for the simulations can be considered satisfactory.

6. CONCLUSIONS

This paper describes a CFD turbine simulation method. First, an assessment was made of the different CFD modeling options, focusing on a description of the turbine used, boundary conditions and turbulence model. The selection of the turbulence model was based on several works in the literature that successfully applied the $\kappa - \omega$ SST model to turbomachinery simulations. As boundary conditions, total pressure and temperature were imposed in the inlet cross-section and static pressure at the domain outlet throughout the work. A description of the experimental facility and the measuring sensors used to acquire the validation data was also given. To optimize the distribution of cells in the mesh, a new procedure was developed to analyze mesh independence. The general mesh independence procedure is based on analyzing the total number of cells in the mesh. In this work, the analysis was performed by dividing the turbine into zones: the volute, stator, rotor, and outlet regions. The cell size of each zone was varied and replaced in a reference case until the independence of the current region was achieved. The same procedure was repeated for the different regions. Using this new strategy, a more appropriate cell distribution can be obtained than that provided by a standard mesh independence analysis. One possible limitation of this procedure is that it assumes that the mesh independence analysis of each subdomain does not depend on the mesh in the other regions. This problem was addressed in the paper, and the defined mesh was found to fulfill the requirements. It is also important to emphasize that the mesh independence was evaluated under certain operating conditions, and the mesh obtained could vary if these conditions were to change, particularly when working under off-design conditions. However, analyzing the mesh for multiple operating points involves an unacceptable computational cost. This novel procedure has been applied to the case of a radial turbine. However, the methodology could be used for the mesh independence analysis of any complex system.

Next, the different options available in ANSYS-FLUENT for the case configuration were analyzed. These options address solver type, moving mesh strategy and time-step size.

Density- and pressure-based solvers give different results. However, the relative error decreases as the number of cells in the mesh increases. Two different approaches were considered for rotor motion strategy: multiple reference frame and the sliding mesh model. The first approach has a much lower computational cost and gives a good approximation (approximately 7 % error in torque) if the operating point is close to the design conditions and was thus applied to obtain the characteristic curves of the turbine. However, when off-design points are considered, the error increases because the transient effects due to rotor-stator interaction increase, and it is therefore necessary to perform a fully transient simulation and actually rotate the mesh to capture this behavior.

Finally, because a VGT turbine was analyzed, the effect of nozzle aperture on turbine flow capacity and the performance curve was studied. The results were compared with experimental measurements taken from a turbocharger test rig. The agreement between both sets of results validates the computational method developed.

ACKNOWLEDGEMENTS

REFERENCES

1. Aghaei tog R, Tousi AM, Tourani A (2008). Comparison of turbulence methods in CFD analysis of compressible flows in radial turbomachines. *Aircraft Engineering and Aerospace Technology: An International Journal* 80(6):657-665.
2. ANSYS (2009). *Ansys Fluent 12.0 User's Guide*. Canonsburg, PA: ANSYS Inc.
3. ANSYS (2011). *ANSYS FLUENT Theory Guide*. ANSYS Inc.
4. Aymanns R, Scharf J, Uhlmann T, Lückmann D (2011). A revision of quasi steady modelling of turbocharger turbines in the simulation of pulse charged engines. *16th Supercharging Conference*.
5. Baines NC (2005). *Fundamentals of Turbocharging*. Concepts NREC.
6. Baines NC (2010), Turbocharger turbine pulse flow performance and modeling - 25 years on. *9th Int. Conf. Turbochargers and Turbocharging*, 347-362.

7. Baris O, Mendonça F (2011). Automotive turbocharger compressor CFD and extension towards incorporating installation effects. *Proceedings of the ASME Turbo Expo 2011: Power for Land, Sea and Air*, GT2011-46796.

8. Blanco-Marigorta E, Fernández-Francos J, González-Pérez J, Santolaria-Morros C (2000). Numerical flow simulation in a centrifugal pump with impeller-volute interaction. *ASME 2000 Fluids Engineering Division Summer Meeting*.

9. Dai J, Ijichi N, Tange H, Shibata H, Tamaki H, Yamaguchi S (2004). Comparison of internal flow field between experiment and computation in a radial turbine impeller. *JSME International Journal Series B* 47(1):48-56.

10. Decombes G, Pichouron JF, Maroteaux F, Moreno N, Jullien J (2010). Simulation of the performance of a variable geometry turbocharger for diesel engine road propulsion. *International Journal of Thermodynamics* 5(3):139-149.

11. Esch T, Menter FR (2003). Heat transfer predictions based on two-equation turbulence models with advanced wall treatment. *Proceedings of the 4th International Symposium on Turbulence, Heat & Mass Transfer*, Antalya, Turkey, 614-621.

12. FLUENT (2006). FLUENT 6.3 Validation Guide.

13. Galindo J, Serrano JR, Guardiola C, Cervelló C (2006). Surge limit definition in a specific test bench for the characterization of automotive turbochargers. *Experimental Thermal and Fluid Science* 30(5):449-462.

14. Galindo J, Tiseira A, Fajardo P, Navarro R (2011). Coupling methodology of 1D finite difference and 3D finite volume CFD codes based on the method of characteristics. *Mathematical and Computer Modelling* 54(7-8):1738-1746.

15. Galindo J, Fajardo P, Navarro R, García-Cuevas LM (2013). Characterization of a radial turbocharger turbine in pulsating flow by means of CFD and its application to engine modeling. *Applied Energy* 103:116-127.

16. Hellström F, Fuchs L (2008). Effects of inlet conditions on the turbine performance of a radial turbine. *Proceedings of the ASME Turbo Expo 2008: Power for Land, Sea and Air (6)*.

17. Hellström F, Fuchs L (2009). Numerical computation of the pulsatile flow in a turbocharger with realistic inflow conditions from an exhaust manifold. *Proceedings of ASME Turbo Expo 2009: Power for Land, Sea and Air*, GT2009-5961.

18. Hellström F (2010). *Numerical Computations of the Unsteady Flow in Turbochargers*. PhD thesis, Royal Institute of Technology KTH Fluid Physics.

19. Hiereth H, Prenninger P (2007). *Charging the Internal Combustion Engine*. Springer Verlag.

20. Hillewaert K, Van den Braembussche RA (1998). *Numerical Simulation of Impeller-Volute Interaction in Centrifugal Compressors*. ASME Paper No. 98-GT-244.

21. Japikse D, Baines NC (1997). *Introduction to Turbomachinery*. Oxford University Press.

22. Kawakubo T (2010). Unsteady rotor-stator interaction of a radial-inflow turbine with variable nozzle vanes. *Proc. of ASME Turbo Expo 2010: Power for Land, Sea and Air*, GT2010-23677.

23. Kreuz-Ihli T, Filsinger D, Schulz A, Wittig S (2000). Numerical and experimental study of unsteady flow field and vibration in radial in flow turbines. *Journal of Turbomachinery* 122:247-254.

24. Lam JKW, Roberts QDH, McDonnell GT (2002). Flow modelling of a turbocharger turbine under pulsating flow. *ImechE Conference Transactions from 7th International Conference on Turbochargers and Turbocharging*, 14-15.

25. Li H (2009). Fluid flow analysis of a single-stage centrifugal fan with a ported diffuser. *Engineering Applications of Computational Fluid Mechanics* 3:147-163.

26. Liu Z, Hill DL (2000). Issues surrounding multiple frames of reference models for turbo compressor applications. *Fifteenth International Compressor Engineering Conference*, Purdue University, USA.

27. Luján JM, Bermúdez V, Serrano JR, Cervelló C (2002). Test Bench for Turbocharger Groups Characterization. SAE Paper 2002-01-0163.

28. Menter FR (1992). Influence of freestream values on k-omega turbulence model predictions. *AIAA journal* 30:1657-1659.

29. Menter FR (1994). Two-equation eddy-viscosity turbulence models for engineering applications. *AIAA journal* 32(8):1598-1605.

30. Menter FR, Langtry R, Hansen T (2004). CFD simulation of turbomachinery flows verification, validation and modeling. *European Congress on Computational*

Methods in Applied Sciences and Engineering, ECCOMAS.

31. Palfreyman D, Martinez-Botas RF (2005). The pulsating flow field in a mixed flow turbocharger turbine: An experimental and computational study. *Journal of Turbomachinery* 127(1):144-155.

32. Pecnik R, Witteveen JAS, Iaccarino G (2011). Uncertainty quantification for laminar-turbulent transition prediction in RANS turbomachinery applications. *49th AIAA Aerospace Sciences Meeting including the New Horizons Forum and Aerospace Exposition.*

33. Rajoo S, Botas RM (2008). Variable geometry mixed flow turbine for turbochargers: An experimental study. *International Journal of Fluid Machinery and Systems* 1(1):155-168.

34. SAE (1995). *Supercharching Testing Standards.*

35. Simpson AT, Spence SWT, Watterson JK (2009). A comparison of the flowstructures and losses within vaned and vaneless stators for radial turbines. *Journal of Turbomachinery* 131(3), 031010.

36. Smagorinsky J (1963). General circulation experiments with the primitive equations. *Monthly Weather Review* 91(3):99-164.

37. Spence SWT, Rosborough RSE, Artt D, McCullough G (2007). A direct performance comparison of vaned and vaneless stators for radial turbines. *Journal of Turbomachinery* 129(1):53-61.

38. Strelets M (2001). Detached eddy simulation of massively separated flows. *39th AIAA Aerospace Sciences Meeting and Exhibit.*

39. Su WT, Li FC, Li XB, Wei XZ, Zhao Y (2012). Assessment of LES performance in simulating complex 3D flows in turbomachines. *Engineering Applications of Computational Fluid Mechanics* 6(3):356-365.

40. Tabor GR, Baba-Ahmadi MH (2010). Inlet conditions for large eddy simulation: A review. *Computers and Fluids* 39:553-567.

41. Thakker A, Hourigan F (2005). Computational fluid dynamics analysis of a 0.6 m, 0.6 hub-to-tip ratio impulse turbine with fixed guide vanes. *Renewable Energy* 30(9):1387-1399.

42. Torregrosa AJ, Fajardo P, Gil A, Navarro R (2012). Development of a non-reflecting boundary condition for its application in 3D computational fluid dynamic codes. *Engineering Applications of Computational Fluid Mechanics* 6(3):447-460.

43. Tritthart M, Gutknecht D (2007). Three-dimensional simulation of free-surface flows using polyhedral finite volumes. *Engineering Applications of Computational Fluid Mechanics* 1(1):1-14.

44. Wilcox DC (1988). Reassessment of the scale-determining equation for advanced turbulence models. *AIAA Journal* 26(11):1299-1310.